

Ultrafast energy-dispersive soft-x-ray diffraction in the water window with a laser-driven source

J. Jarecki,¹ M. Hennecke,¹ T. Sidiropoulos,¹ M. Schnuerer,¹ S. Eisebitt,^{1,2} and D. Schick^{1, a)}

¹⁾ *Max-Born-Institut für Nichtlineare Optik und Kurzzeitspektroskopie, Max-Born-Straße 2A, 12489 Berlin, Germany*

²⁾ *Technische Universität Berlin, Institut für Optik und Atomare Physik, 10623 Berlin, Germany*

(Dated: 9 July 2024)

Time-resolved soft-x-ray-diffraction experiments give access to microscopic processes in a broad range of solid-state materials by probing ultrafast dynamics of ordering phenomena. While laboratory-based high-harmonic generation (HHG) light sources provide the required photon energies, their limited photon flux is distributed over a wide spectral range, rendering typical monochromatic diffraction schemes challenging. Here, we present a scheme for energy-dispersive soft-x-ray diffraction with femtosecond temporal resolution and photon energies across the water window from 200 eV to 600 eV. The experiment utilizes the broadband nature of the HHG emission to efficiently probe large slices in reciprocal space. As a proof-of-concept, we study the laser-induced structural dynamics of a Mo/Si superlattice in an ultrafast, non-resonant soft-x-ray diffraction experiment. We extract the underlying strain dynamics from the measured shift of its 1st order superlattice Bragg peak in reciprocal space at photon energies around 500 eV via soft-x-ray scattering simulations.

I. INTRODUCTION

Soft-x-ray radiation is highly sensitive to a wide range of phenomena in physics, chemistry, biology, and material science. By covering core-to-valence resonances, it can spectroscopically probe charge, spin, and orbital degrees of freedom in various material systems with element sensitivity^{1,2}. For solid-state research, the short wavelengths also enable few-nanometer spatial resolution, e.g., via diffraction and imaging techniques³⁻⁷, and exhibit considerable penetration depth, rendering soft-x-ray techniques eligible for studying nanoscale heterostructures and buried layers⁸⁻¹⁰. In addition to accelerator-based installations at free-electron lasers and synchrotron-radiation facilities, laser-driven high-harmonic generation (HHG) is becoming increasingly popular as a source of short-wavelength radiation spanning from the extreme ultraviolet (XUV)¹¹⁻¹³ into the water-window, ranging from the C *K*-edge at 284 eV up to the O *K*-edge at 531 eV and beyond^{14,15}. The HHG's properties, such as spectrum, polarization, and pulse duration, are directly controlled by the driving laser and medium^{16,17}, facilitating the application of diverse experimental techniques with a temporal resolution down to the attosecond regime¹⁸⁻²¹. The key to reaching the soft-x-ray photon energy range by HHG is to increase the driving laser wavelength λ_1 , which at the same time leads to a severe decrease of the HHG efficiency scaling with $\lambda_1^{-(5-6)}$ ²²⁻²⁴. Furthermore, the achievable, comparatively small photon flux is also distributed over a broad spectral range, typically spanning hundreds of electron volts (eV)²⁵⁻²⁷. This broadband emission renders HHG sources in the soft-x-ray range ideally suited for broadband absorp-

tion spectroscopy techniques, which have been successfully demonstrated in a series of ground-breaking experiments mainly targeting local atomic and molecular dynamics²⁸⁻³¹. Diffraction experiments, however, which can provide access to nanoscale long-range order, typically require extremely photon-inefficient monochromatization of the broad HHG spectra³². As a result, time-resolved diffraction experiments within the water window employing HHG sources have been elusive so far. Here, we show how to benefit from the broadband and quasi-continuous nature of HHG spectra in soft-x-ray diffraction experiments by realizing an energy-dispersive scheme^{33,34} for efficiently probing large slices in reciprocal space. We utilize femtosecond, broadband soft-x-ray pulses ranging from 200 eV to 600 eV to enable time-resolved diffraction experiments at around 500 eV for the first time at an HHG-based setup. For this proof-of-concept experiment, we study the photoinduced structural dynamics of a Mo/Si superlattice (SL) in non-resonant, specular diffraction geometry. We observe a shift of the SL's 1st order Bragg peak in reciprocal space on a few picosecond time scale. A combination of ultrafast thermo-elastic and x-ray-scattering simulations can fully reproduce these experimental results, enabling direct and quantitative access to the underlying coherent motion of the atomic lattice. Our findings demonstrate the feasibility and sensitivity of the energy-dispersive diffraction approach, especially for probing Bragg peak shifts in reciprocal space, independent of the HHG pulse-to-pulse intensity fluctuations. Extending the applicability of HHG-driven soft-x-ray sources in this high photon-energy range will enable a variety of time-resolved diffraction experiments on ordering phenomena of electronic, structural, and magnetic origin³⁵⁻³⁸.

^{a)} Electronic mail: schick@mbi-berlin.de

II. RESULTS & DISCUSSION

The general concept of our soft-x-ray diffraction experiment, combining a common $\theta/2\theta$ diffractometer with a spectrometer³⁹, is sketched in Fig. 1(a). As HHG driver, we employ a high-average-power mid-infrared (MIR) optical parametric chirped pulse amplifier (OPCPA) system operating at a repetition rate of 10 kHz providing pulses of 27 fs (full width at half maximum, FWHM) duration at a central wavelength of $2.1\ \mu\text{m}$ ⁴⁰. The laser pulses are focused into a He gas cell at a backing pressure of 2.3 bar and subsequently generate soft-x-ray pulses of ≤ 27 fs FWHM duration spanning a broad spectral range from 200 eV to 600 eV. The soft-x-ray probe pulses impinge on the sample under a grazing angle θ and get scattered into the rotatable spectrometer at an angle of 2θ with respect to the incident beam. The spectrometer consists of a variable-line-spacing grating (VLS) and an in-vacuum CCD camera, which provide a spectral resolution of about 1 eV at a photon energy, E_{ph} , of 500 eV. A typical soft-x-ray spectrum after transmission through two Al filters of a total thickness of 500 nm fully covering the water window is depicted in Fig. 1(b). Absolute photon numbers have been determined with calibrated detection equipment previously⁴¹. In the spectrum, several absorption lines corresponding to K -edges of residual molecules of C (285 eV and 292 eV⁴²), N (409.9 eV¹⁵), and O (531 eV and 538 eV⁴³), can be identified and utilized for energy calibration of the spectrometer. A 8%-fraction of the $2.1\ \mu\text{m}$ laser light is split off and guided via a mechanical delay line to the sample for photoexcitation. A rotatable waveplate and polarizer set the incident fluence to $9\ \text{mJ}/\text{cm}^2$. Due to the non-collinearity of 3.3° between the pump and the probe pulses and their spot sizes at normal incidence of $543\ \mu\text{m} \times 317\ \mu\text{m}$ FMWH and $77\ \mu\text{m} \times 111\ \mu\text{m}$ FMWH, respectively, we achieve a temporal resolution of about 40 fs. Both the pump and probe pulses are p -polarized with respect to the scattering plane.

In a diffraction experiment probing the sample's out-of-plane (OOP) order along the z -direction, the magnitude of the corresponding scattering vector, $Q_z = |\vec{Q}| = |\vec{k}_{\text{out}} - \vec{k}_{\text{in}}|$, is defined as

$$Q_z = \frac{4\pi E_{\text{ph}}}{h c_0} \sin \theta, \quad (1)$$

where h denotes the Planck constant and c_0 is the speed of light in vacuum. In order to access an OOP periodicity d , a multiple of its corresponding reciprocal lattice vector $|\vec{G}| = \frac{2\pi}{d}$ must match the scattering vector \vec{Q} , as described by the Laue condition:

$$\vec{Q} = \vec{k}_{\text{out}} - \vec{k}_{\text{in}} = n\vec{G}. \quad (2)$$

Here, $\vec{k}_{\text{in/out}}$ denote the wavevectors of the incident and scattered soft-x-ray light, respectively, and n is an integer number corresponding to the diffraction order. Typ-

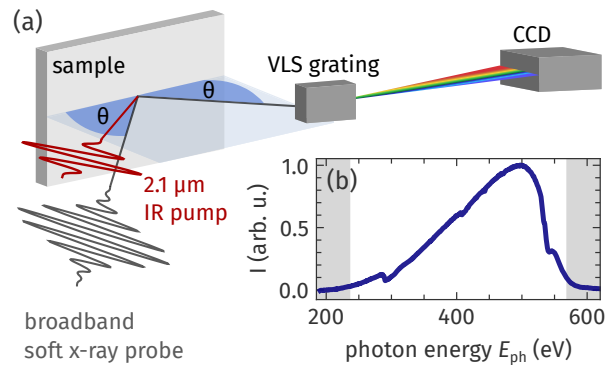


FIG. 1. (a) Setup for time-resolved energy-dispersive soft-x-ray diffraction utilizing an HHG source. The broadband soft-x-ray pulses hit the sample at a variable grazing angle θ and are scattered specularly off the sample. The rotatable spectrometer combines a variable-line-spacing (VLS) grating and a CCD camera to detect scattered soft-x-ray radiation with photon energy resolution. The $2.1\ \mu\text{m}$ -MIR pulses excite the sample quasi-collinearly with the probe pulses. (b) Typical soft-x-ray spectrum emitted by the HHG source ranging from 200 eV to 600 eV. The grey areas mark the spectral regions which are omitted in the analysis due to insufficient photon flux.

ical monochromatic diffraction schemes comprise time-consuming variations of θ and/or E_{ph} for scanning reciprocal space, rendering themselves inconvenient and inefficient for broadband HHG sources in the water window. The concept of probing diffraction in an energy-dispersive mode circumvents this requirement and enables access to large reciprocal-space volumes very photon- and time-efficiently in a single acquisition (see Supplemental Material).

To demonstrate the capabilities of the approach and experimental realization, we study the laser-induced structural dynamics of a Mo/Si superlattice, a material system which allows to realize efficient mirrors in the XUV and soft-x-ray spectral range^{44–46}. The particular sample structure presented in this paper has already been investigated in a previous study, focusing on its use as a cross-correlator for optical laser pulses with soft-x-ray pulses at a broad range of photon energies⁴⁷. The SL is built of 40 double layers (DL) of 1.88 nm polycrystalline Mo and 2.05 nm amorphous Si on a crystalline Si substrate (see Fig. 2(d)). The artificial unit cell of the SL is defined by the double-layer thickness $d_{\text{DL}} = 3.93$ nm and the corresponding reciprocal lattice vector $G_{\text{DL}} = 2\pi/d_{\text{DL}}$. The structural parameters have been extracted and refined by comparing static synchrotron data with matrix-formalism-based x-ray-scattering simulations^{48,49} (see Supplemental Material).

We use the same simulations to model the x-ray-scattering signal from the Mo/Si SL in our energy-dispersive setup in Fig. 2(a). We show the static result for the same angular and photon-energy range accessible in the experiment, which in principle gives access to

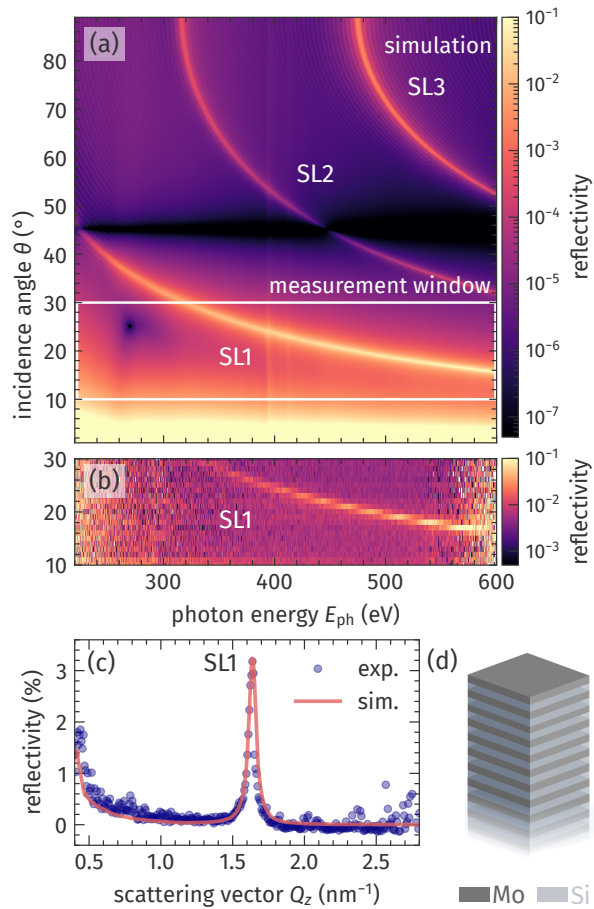


FIG. 2. Energy-resolved soft-x-ray diffraction from the Mo/Si superlattice (SL) structure. (a) Simulated x-ray-scattering signal of the Mo/Si SL structure [see panel (d)] with varying incidence angle θ and photon energy E_{ph} . Soft-x-ray light diffracted from the periodically ordered Mo/Si layers results in distinct intensity peaks, i.e. SL Bragg peaks of order n (SL n). (b) Measurement of the diffraction signal employing broadband soft-x-ray pulses under variation of the incidence angle θ from 10° to 30° as highlighted by the white box in panel (a). (c) The simulated and experimental data from (a) and (b) are transformed into reciprocal space, revealing the 1st order SL Bragg peak.

three SL Bragg peaks of the order $n = 1, 2, 3$. While the SL Bragg peaks appear at fixed scattering vectors \vec{Q} in reciprocal space, they can be accessed by different combinations of the incidence angle θ and the photon energy E_{ph} in real-space coordinates according to Eq. (1). In Fig. 2(b), we show the experimental, energy-dispersed scattering intensity for incidence angles θ in the range of 10° to 30° with a step size of 1° . The experimental spectra are obtained from 5 s-integrations for each angle, resulting in a reasonably short acquisition time of the total scan. Based on the high spectral stability of our HHG source, we can normalize the experimental data of a total angle scan to the source spectrum as shown in

Fig. 1(b). As a result, the experimental data is intrinsically self-normalized within every acquisition, providing accurate *relative* intensities of diffraction signals. However, because we lack an online monitor for the integrated intensity of the HHG, we do not rely on the *absolute* amplitude of the diffraction signal. Instead, we scale all acquired spectra of a scan to match the absolute intensities of the reliable x-ray-scattering simulations of the high-quality Mo/Si SL. This procedure does not influence the SL Bragg positions. The measured data agrees very well with the expected shift of the SL1 Bragg peak in photon energy with varying θ . This static result already highlights the sensitivity and efficiency of the energy-dispersive diffraction approach to capture large slices in reciprocal space in a single acquisition.

For a quantitative comparison of the simulation and experimental data from panels (a) and (b) of Fig. 2, we convert both datasets into reciprocal space, following Eq. (1). This transformation for all photon energies at every θ position results in a diffraction profile with a Bragg peak appearing at the same specific scattering vector Q_z . To enable proper averaging of the diffraction data along the θ -axis it is necessary to map the data of each scan onto the same regular Q_z -grid, as scanning the incidence angle leads to a shift and a different spacing of the probed reciprocal-space volume⁵⁰. In Fig. 2(c) we show the averaged experimental data (blue symbols) together with the simulation (red solid line) after the Q_z -transformation. In the analysis of both the experimental data and the simulation, we consider only the spectral range of sufficiently high soft-x-ray intensity in the experiment between 230 eV to 570 eV [non-shaded area in Fig. 1(b)]. We achieve an excellent agreement between experiment and simulation by adjusting only the absolute angle of incidence θ by a small offset of 0.5° and scaling the measured intensities by a single factor for all spectra as described above. We observe the 1st order SL Bragg peak at $Q_z = 1.626 \text{ nm}^{-1}$, which is clearly shifted with respect to the predicted value following the Laue condition, c.f. Eq. (2), at $Q_z^{\text{Laue}} = G_{\text{DL}} = 1.599 \text{ nm}^{-1}$. It has been shown, that this offset can be attributed to refraction effects introducing different phase shifts between interfering wavefronts as compared to the hard-x-ray range, resulting in the shifted Bragg peak position^{8,51–53}. Next, we measure the laser-induced response of the Mo/Si SL in a pump-probe experiment with femtosecond temporal resolution. The laser-driven dynamics of the Mo/Si SL can be expected to evolve as follows⁴⁷: The laser energy is mainly absorbed by the metallic Mo layers, whereas the semiconductor Si is transparent for the 2.1 μm -pump-laser pulses. This results in an alternating pattern of quasi-instantaneously heated and cold SL layers with an exponentially decaying excitation amplitude along the depth of the sample. This ultrafast heating leads to a rapid expansion of the Mo sub-lattice while the cold Si layers get compressed, leading to a complex pattern of zone-folded longitudinal acoustic phonons (ZFLAPs)^{54,55} within the SL. On top of this sub-ps oscillatory dynamics,

a bipolar strain wave is launched from the surface of the SL towards its lower interface^{56–58}. The picosecond time scale of this coherent strain-wave propagation is unambiguously determined by the acoustic sound velocity and thickness of the Mo/Si SL. Simultaneously, Si also starts to expand once energy is transferred via phononic heat diffusion between the few-nanometer-thin layers of Mo and Si, resulting in an increased double-layer thickness according to the laser-induced temperature rise in both materials. On nanosecond time scales, the SL starts to relax back to its equilibrium via heat transport to the substrate^{47,59}.

In the transient, energy-dispersive diffraction experiment, we probe the evolution of the SL1 Bragg peak at a fixed incidence angle of $\theta = 19^\circ$ to particularly follow the propagation of the coherent longitudinal strain wave described above. The presented delay scan comprises 12 loops of 30 s integration at each delay point resulting in a total measurement duration of about 4 h. The experimental data, as shown in Fig. 3(a), reveal an increasing transient shift of the SL1 Bragg peak to smaller scattering vectors Q_z or smaller photon energies E_{ph} . This shift can be qualitatively understood as a direct transla-

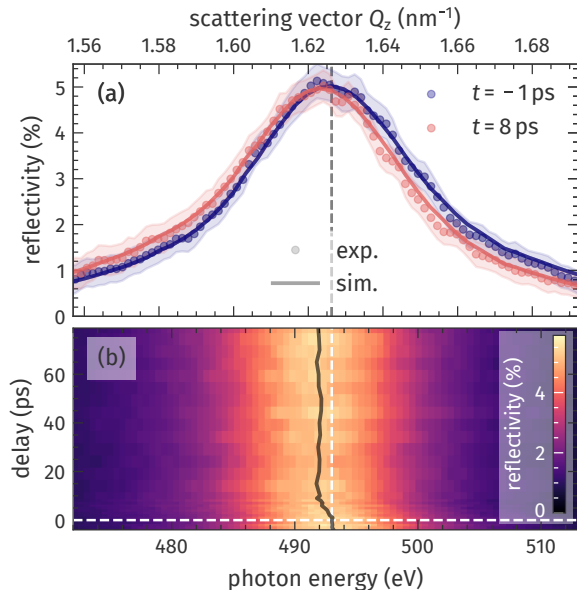


FIG. 3. Transient energy-dispersive diffraction from the Mo/Si superlattice. (a) The 1st order SL Bragg peak before and after laser excitation shifts along Q_z in reciprocal space or equivalently in energy in real space. Solid lines represent the modeled x-ray-scattering signal and circles the experimental data at a fixed angle of incidence $\theta = 19^\circ$. The shaded area is defined by the standard error of each data point representing the uncertainty of the measurement at both delays. (b) Full map of energy-dispersive reciprocal-space scans for pump-probe delays ranging from -4 ps to 79 ps. The extracted Bragg peak position (black solid line) clearly reveals even small transient shifts in reciprocal space. Both panels share the scattering vector and photon-energy axis.

tion of the laser-driven lattice expansion into reciprocal space via the Laue condition [Eq. (2)]. For the complete transient dataset, as shown in panel (b), we extract the SL1 Bragg peak position by Gaussian fits (solid black line). To gain quantitative insights into the laser-driven lattice dynamics, we use the UDKM1DSIM toolbox⁴⁹ to simulate the thermo-elastic response of the Mo/Si SL. To that end, we first calculate the pump laser’s absorption profile according to the multi-layer absorption formalism to determine the initial spatial energy distribution. In the second step, we use a Fourier heat-diffusion model to calculate the spatio-temporal temperature rise in the sample. This temperature map can be used to obtain the transient strain response by solving a linear-chain model of masses and springs. The details and parameters of these simulations are given in the Supplemental Material. In the final step, the structural dynamics are fed as input into the same x-ray-scattering formalism, which has been benchmarked by the static HHG and synchrotron data [Fig. 2(a)] to model the transient, energy-dispersive x-ray-diffraction signal. Using literature values for the thermo-elastic sample parameters (see Supplementary Material) and with the laser-excitation fluence as the only free parameter, we can fully simulate the shift of the SL1 Bragg peak, as shown by the solid lines in Fig. 3(a) for the two selected delays.

In Fig. 4(a), we show the full temporal evolution of the relative SL1 Bragg peak position $\Delta E/E(t < 0 \text{ ps})$ extracted from both the transient experimental as well as the simulated scattering signals. The analysis shows that the amplitude of the relative Bragg peak shift is superimposed by modulations of the transient signal, which can be attributed to the propagating strain wave generated by ultrafast laser heating. However, comparing the transient relative peak shift to the strain averaged across the entire SL depth [blue line in Fig. 4(b)] reveals substantial differences. The modeled strain response indicates the bipolar strain wave arriving at the SL-substrate interface after 26 ps, where it is partially reflected, resulting in a short modulation of the average lattice strain. In contrast, the experimental peak shift reflects the relative change of the DL thickness across the probing depth of the soft-x-ray light, which is significantly shorter than the entire SL thickness of 157 nm. Consequently, the peak-shift signal probes only the arrival of the reflected strain wave at the surface after 52 ps while the substrate interface at a depth of 157 nm is not accessible. Moreover, the observed peak shift exceeds the fitted average strain of the Mo/Si SL nearly by a factor of two. Both effects can be understood by comparing the SL peak shift to the weighted averaged strain assuming an exponentially decaying absorption profile of the soft-x-rays [red line in Fig. 4(b)]. We extract this probing depth to be 65 nm and taking that information depth into account the resulting weighted strain perfectly matches the relative peak shift observed in the experiment as seen in Fig. 4(a).

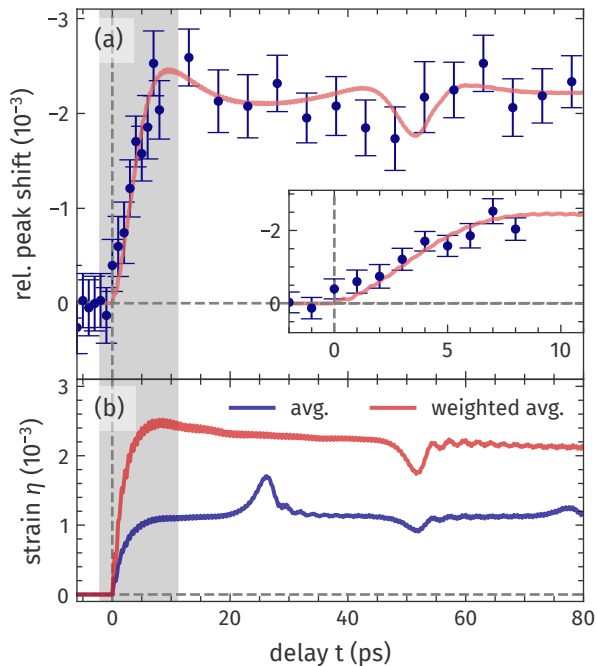


FIG. 4. Temporal evolution of the lattice dynamics within the Mo/Si superlattice. (a) The extracted relative shift of the SL1 Bragg peak from the experimental (symbols) and simulated (solid line) x-ray diffraction. The inset displays a detailed view on the initial lattice dynamics marked by the shaded area. The error bars correspond to the statistical standard error. (b) Simulated average strain of the full Mo/Si SL (blue line) and weighted by the soft-x-ray absorption profile at 500 eV (red line).

III. CONCLUSION

To the best of our knowledge, we presented the first time-resolved diffraction experiment within the water window around 500 eV photon energy at a laser-driven HHG source. The combination of a broadband soft-x-ray source with an energy-dispersive diffractometer enables fast and efficient access to large slices in reciprocal space. We have demonstrated the feasibility of this experimental scheme by probing the 1st order Bragg peak of a Mo/Si SL both statically and temporally resolved after laser excitation with 40 fs temporal resolution enabled by reasonable short acquisition times facilitating pump-probe experiments. We obtain excellent agreement between the static as well as transient experimental data with x-ray scattering simulations. In both experiment and theory, the underlying structural information is accessible by analyzing the corresponding Bragg peak shape in reciprocal space. This combined experimental and theoretical approach enables an unambiguous and quantitative determination of the underlying spatio-temporal strain dynamics in the Mo/Si SL after photoexcitation on the femto- and picosecond time scale.

Based on the high stability of the spectral shape of

our HHG source, we can follow Bragg peak shifts with remarkable sensitivity. The future implementation of intensity-normalization schemes^{60,61} will enable a new class of experiments that are also sensitive to ultrafast changes of the structure factors associated with nanoscale periodicities. Beyond this experimental proof-of-concept focused on probing the coherent acoustic lattice dynamics in a Mo/Si SL, transient and energy-dispersive diffraction experiments at HHG sources as demonstrated here will be able to target other order phenomena of spin, charge, and orbital origin. This does require reaching the relevant core-to-valence transitions of the elements involved, in order to provide sufficient diffraction contrast. Our state-of-the-art setup reaches the *L*-edges of the early 3d transition metals, such as Ti and V, as well as the *K*-edges of O, which already now enables a variety of studies within the broad class of oxide materials. With new powerful laser systems at even longer driver wavelengths at the horizon, the *L*-edges of other, e.g., magnetically relevant elements such as Mn, Co, Fe, and Ni will also become within reach for energy-dispersive diffraction experiments at laser-driven HHG sources.

ACKNOWLEDGMENTS

J.J. and D.S. would like to thank the Leibniz Association for funding through the Leibniz Junior Research Group J134/2022. This work was carried out at the Nanomovie Application Laboratory at the Max Born Institute, which was established with the help of the European Regional Development Fund.

Appendix A: Energy-dispersive diffraction with a white-light source

In this section, we illustrate the concept of energy-dispersive diffraction compared to common monochromatic diffraction schemes. In a diffraction experiment probing the sample's out-of-plane (OOP) order along the *z*-direction, the magnitude of the probed scattering vector, defined as the difference between the wave vectors of the incident and scattered soft-x-ray light $Q_z = |\vec{Q}| = |\vec{k}_{\text{out}} - \vec{k}_{\text{in}}|$, is determined by the photon energy E_{ph} and its incidence angle θ :

$$Q_z = \frac{4\pi E_{\text{ph}}}{h c_0} \sin \theta, \quad (\text{A1})$$

where h denotes the Planck constant and c_0 is the speed of light in vacuum. Therefore, a scan of the reciprocal space can be obtained by either varying θ , that changes the wave vectors' direction but keeping their magnitude fixed [see Fig. 5(a)], or by varying E_{ph} , which changes the magnitude of $\vec{k}_{\text{out}} - \vec{k}_{\text{in}}$ [see Fig. 5(b)]. Both methods provide the desired result, but employing white-light sources to common specular reflection geometries and

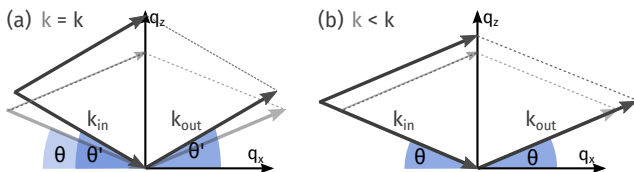


FIG. 5. Scanning reciprocal space can be realized by varying the incidence angle (a) or the photon energy, which changes the length of the wave vector of the light (b).

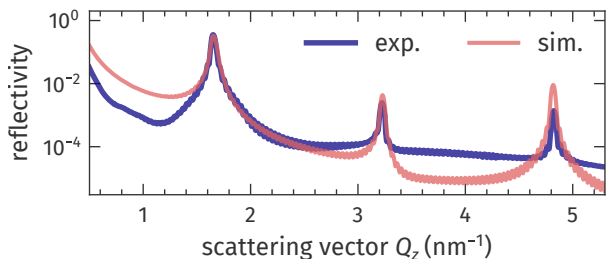


FIG. 6. The simulated soft-x-ray scattering intensity as function of scattering vector Q_z is compared to an experimental Q_z scan measured in a monochromatic diffraction experiment at $E_{\text{ph}} = 1200$ eV.

adding an energy-dispersive detection increases the efficiency regarding acquisition time by enabling probing of large slices of reciprocal space in a single acquisition.

Appendix B: Sample calibration via soft-x-ray simulations

In this section, we describe the procedure of extracting the superlattice (SL) parameters by modeling the static Mo/Si SL soft-x-ray scattering response in reciprocal space and comparing it to an extended Q_z -scan measured in a soft-x-ray diffraction experiment at the PM3 beamline at BESSY II. The experimental data shown in Fig. 6(a) has been published previously⁴⁷, whereas the simulations are refined by a soft-x-ray scattering formalism^{48,49}. The Q_z -scan has been obtained by varying the incident angle of the monochromatic soft-x-ray radiation at a fixed photon energy $E_{\text{ph}} = 1200$ eV, which leads to a variation of the probed scattering vector Q_z , c.f. Eq. (1). The probed Q_z -interval displays three distinct SL Bragg peaks of the order $n = 1, 2, 3$. In the modeling, we first determined the thickness of the Mo/Si double-layer d_{DL} , that defines the reciprocal lattice vector $|\vec{G}_{\text{SL}}| = 2\pi/d_{\text{DL}}$ and therefore the position of the SL Bragg peaks in reciprocal space. The intensity peaks of consecutive order are separated by \vec{G}_{SL} , which allows for a precise determination of the real space DL thickness. In a second step, we refined the sublayer thicknesses d_i of the constituent SL materials Mo and Si. The ratio $d_{\text{Mo}}/d_{\text{Si}}$ can be understood as the SL form factor, which determines the scattered intensity amplitude for each SL Bragg peak

of the order n . We obtained the best result using the parameters summarized in the top part of Table I providing a reasonable agreement of the experimental and simulated data for the first and second SL Bragg peak. As discussed in Ref.⁴⁷, deviations between the measured and simulated peak intensities, that occur for higher order SL peaks, can be attributed to thin inter-diffusion layers of MoSi₂ between the Mo and Si layers in the SL structure.

Appendix C: Ultrafast SL strain response upon laser excitation

In this section, we briefly describe the modeling of the laser-induced change of the SL diffraction signal upon laser excitation in a purely one-dimensional treatment of the sample using the udkm1Dsim toolbox⁴⁹ and the layer-specific parameters given in Table I. The ultrafast excitation of the SL induces an ultrafast strain response of the lattice, leading to the temporal changes of the soft-x-ray scattering signal, which can be captured by the following steps: First, we model the initial energy deposition by the 2.1 μm pump laser pulse according to a multi-layer matrix formalism. As Si is transparent for the IR pulses used in the experiment, Mo is essentially absorbing the excitation light [see Fig. 7(b)]. From this initial depth-dependent energy distribution, we calculate the spatio-temporal temperature map shown in Fig. 7(c) using a Fourier-heat-diffusion model. Due to the large band gap in Si and a fast electron-phonon coupling, that enables a fast equilibration of electrons and phonons in Mo⁷⁵, we can describe the temperature dynamics by a single temperature corresponding to the phonon system of each material. In the next step, we use these time- and depth-dependent temperatures to simulate the ultrafast strain response by numerically solving a linear-chain model of masses and springs. We consider a Poisson-corrected linear thermal expansion coefficient, i.e. the ultrafast expansion coefficient, for both materials. The thermal expansion coefficient as well as the Poisson-factor of Mo are highly temperature-dependent, which is roughly taken into account by increasing both parameters in the model by an offset. The complex spatio-temporal strain map shown in Fig. 7(d) is composed of a quasi-static expansion and coherently driven propagating strain pulses. We can identify the increasing background strain, that is of high amplitude near the surface according to the spatio-temporal temperature rise. Further, we observe a pronounced bipolar strain wave generated near the SL surface, that propagates towards the Si substrate interface, where it gets partially reflected after 25 ps. These structure dynamics are then translated to a time-dependent soft-x-ray scattering signal of the sample using the same x-ray scattering formalism as used for the static case.

	Mo	Si SL	Si substrate
thickness d (nm)	1.88	2.05	615.00
density ρ (g cm^{-3})	9.252	2.336	2.336
heat capacity C ($\text{J kg}^{-1} \text{K}^{-1}$)	250 ⁶²	712 ⁶³	712
therm. conductivity κ ($\text{W m}^{-1} \text{K}^{-1}$)	139 ⁶⁴	1.8 ⁶⁵	149 ⁶⁶
corrected lin. therm. expansion α (10^{-6}K^{-1})	9.86 ^{67,68}	4.25 ^{69,70}	7.08 ^{69,70}
sound velocity v_s (nm ps^{-1})	6.19	8.15 ⁷¹	9.4
refractive index n ($2.1 \mu\text{m}$)	$3.3239 + 19.239j$ ⁷²	$3.4492 + 0j$ ⁷³	$3.4478 + 0j$ ⁷⁴

TABLE I. Thermo-elastic parameters of the Mo/Si superlattice

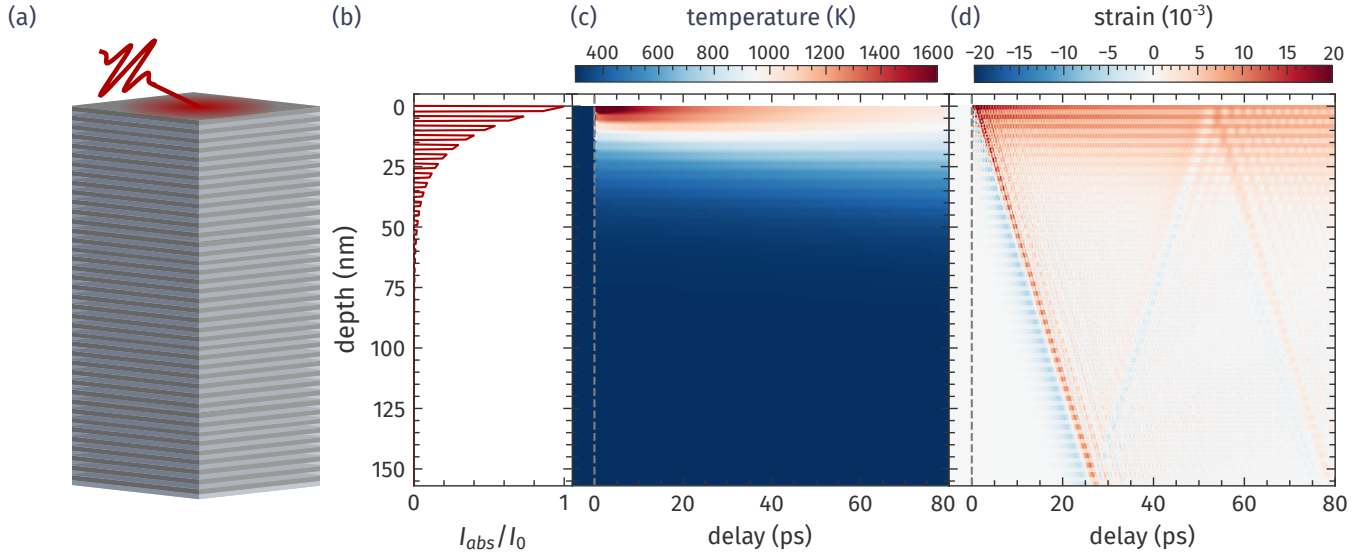


FIG. 7. (a) The Mo/Si SL is built of alternating layers of Mo and Si. (b) The metallic Mo mainly absorbs the IR pump energy resulting in an ultrafast heating of the metal layers. (c) The modeled spatio-temporal temperature map shows ultrafast heating of the excited SL layers and a slow heat transfer into the sample depth. (d) The rapid temperature increase induces a complex spatio-temporal strain response, that is composed of a quasi-static expansion and propagating strain waves.

¹C. Bressler and M. Chergui, “Ultrafast x-ray absorption spectroscopy,” *Chem. Rev.* **104**, 1781–1812 (2004).

²J. Fink, E. Schierle, E. Weschke, and J. Geck, “Resonant elastic soft x-ray scattering,” *Rep. Prog. Phys.* **76**, 056502 (2013).

³J. B. Kortright, S.-K. Kim, G. P. Denbeaux, G. Zeltzer, K. Takano, and E. E. Fullerton, “Soft-x-ray small-angle scattering as a sensitive probe of magnetic and charge heterogeneity,” *Phys. Rev. B* **64**, 092401 (2001).

⁴S. Eisebitt, J. Lüning, W. Schlotter, M. Lörger, O. Hellwig, W. Eberhardt, and J. Stöhr, “Lensless imaging of magnetic nanostructures by x-ray spectro-holography,” *Nature* **432**, 885–888 (2004).

⁵H. N. Chapman and K. A. Nugent, “Coherent lensless x-ray imaging,” *Nature Photon.* **4**, 833–839 (2010).

⁶D. F. Gardner, M. Tanksalvala, E. R. Shanblatt, X. Zhang, B. R. Galloway, C. L. Porter, R. Karl Jr, C. Bevis, D. E. Adams, H. C. Kapteyn, et al., “Subwavelength coherent imaging of periodic samples using a 13.5 nm tabletop high-harmonic light source,” *Nature Photon.* **11**, 259–263 (2017).

⁷J. Reinhard, S. Kaleta, J. J. Abel, F. Wiesner, M. Wünsche, E. Seemann, M. Westermann, T. Weber, J. Nathanael, A. Il'io, et al., “Laboratory-based correlative soft x-ray and fluorescence microscopy in an integrated setup,” *Microsc. Microanal.* **29**, 2014–2025 (2023).

⁸H. Wadati, D. Hawthorn, J. Geck, T. Higuchi, Y. Hikita, H. Hwang, L. Kourkoutis, D. Muller, S.-W. Huang, D. Huang, et al., “Resonant soft x-ray scattering studies of interface re-

constructions in sratio3/laalo3 superlattices,” *J. Appl. Phys.* **106** (2009), 10.1063/1.3246788.

⁹J.-S. Lee, Y. Xie, H. Sato, C. Bell, Y. Hikita, H. Hwang, and C.-C. Kao, “Titanium dxy ferromagnetism at the laalo3/sratio3 interface,” *Nature Mater.* **12**, 703–706 (2013).

¹⁰F. Wiesner, M. Wünsche, J. Reinhard, J. J. Abel, J. Nathanael, S. Skruszewicz, C. Rödel, S. Yulin, A. Gawlik, G. Schmidl, et al., “Material-specific imaging of nanolayers using extreme ultraviolet coherence tomography,” *Optica* **8**, 230–238 (2021).

¹¹L.-O. Chan, M. Siemens, M. M. Murnane, H. C. Kapteyn, S. Mathias, M. Aeschlimann, P. Grychtol, R. Adam, C. M. Schneider, J. M. Shaw, et al., “Ultrafast demagnetization dynamics at the m edges of magnetic elements observed using a tabletop high-harmonic soft x-ray source,” *Phys. Rev. Lett.* **103**, 257402 (2009).

¹²F. Willems, C. T. L. Smeenk, N. Zhavoronkov, O. Kornilov, I. Radu, M. Schmidbauer, M. Hanke, C. von Korff Schmising, M. J. J. Vrakking, and S. Eisebitt, “Probing ultrafast spin dynamics with high-harmonic magnetic circular dichroism spectroscopy,” *Phys. Rev. B* **92**, 220405 (2015).

¹³M. E. Siemens, Q. Li, R. Yang, K. A. Nelson, E. H. Anderson, M. M. Murnane, and H. C. Kapteyn, “Quasi-ballistic thermal transport from nanoscale interfaces observed using ultrafast coherent soft x-ray beams,” *Nat. Materials* **9**, 26–30 (2010).

¹⁴C. Spielmann, N. Burnett, S. Sartania, R. Koppitsch, M. Schnurer, C. Kan, M. Lenzner, P. Wobrauschek, and F. Krausz, “Generation of coherent x-rays in the water window

- using 5-femtosecond laser pulses,” *Science* **278**, 661–664 (1997).
- 15 S. M. Teichmann, F. Silva, S. Cousin, M. Hemmer, and J. Biegert, “0.5-keV soft x-ray attosecond continua,” *Nature Commun.* **7**, 11493 (2016).
 - 16 A. L’Huillier and P. Balcou, “High-order harmonic generation in rare gases with a 1-ps 1053-nm laser,” *Phys. Rev. Lett.* **70**, 774–777 (1993).
 - 17 R. Geneaux, H. J. Marroux, A. Guggenmos, D. M. Neumark, and S. R. Leone, “Transient absorption spectroscopy using high harmonic generation: a review of ultrafast x-ray dynamics in molecules and solids,” *Phil. Trans. R. Soc. A* **377**, 20170463 (2019).
 - 18 P.-M. Paul, E. S. Toma, P. Breger, G. Mullot, F. Augé, P. Balcou, H. G. Muller, and P. Agostini, “Observation of a train of attosecond pulses from high harmonic generation,” *Science* **292**, 1689–1692 (2001).
 - 19 F. Krausz and M. Ivanov, “Attosecond physics,” *Rev. Mod. Phys.* **81**, 163–234 (2009).
 - 20 M. Kretschmar, A. Hadjipittas, B. Major, J. Tümmler, I. Will, T. Nagy, M. Vrakking, A. Emmanouilidou, and B. Schütte, “Attosecond investigation of extreme-ultraviolet multi-photon multi-electron ionization,” *Optica* **9**, 639–644 (2022).
 - 21 M. Kretschmar, E. Svirplys, M. Volkov, T. Witting, T. Nagy, M. J. Vrakking, and B. Schütte, “Compact realization of all-attosecond pump-probe spectroscopy,” *Sci. Adv.* **10**, eadk9605 (2024).
 - 22 M. Lewenstein, P. Balcou, M. Y. Ivanov, A. L’Huillier, and P. B. Corkum, “Theory of high-harmonic generation by low-frequency laser fields,” *Phys. Rev. A* **49**, 2117–2132 (1994).
 - 23 J. Tate, T. Augustine, H. G. Muller, P. Salières, P. Agostini, and L. F. DiMauro, “Scaling of wave-packet dynamics in an intense midinfrared field,” *Phys. Rev. Lett.* **98**, 013901 (2007).
 - 24 A. D. Shiner, C. Trallero-Herrero, N. Kajumba, H.-C. Bandulet, D. Comtois, F. Légaré, M. Giguère, J.-C. Kieffer, P. B. Corkum, and D. M. Villeneuve, “Wavelength scaling of high harmonic generation efficiency,” *Phys. Rev. Lett.* **103**, 073902 (2009).
 - 25 C. Schmidt, Y. Pertot, T. Balciunas, K. Zinchenko, M. Matthews, H. J. Wörner, and J.-P. Wolf, “High-order harmonic source spanning up to the oxygen k-edge based on filamentation pulse compression,” *Opt. Express* **26**, 11834–11842 (2018).
 - 26 J. Pupeikis, P.-A. Chevreuil, N. Bigler, L. Gallmann, C. R. Phillips, and U. Keller, “Water window soft x-ray source enabled by a 25 w few-cycle 2.2 μm OPCPA at 100 kHz,” *Optica* **7**, 168–171 (2020).
 - 27 Y. Fu, K. Nishimura, R. Shao, A. Suda, K. Midorikawa, P. Lan, and E. J. Takahashi, “High efficiency ultrafast water-window harmonic generation for single-shot soft x-ray spectroscopy,” *Commun. Phys.* **3**, 92 (2020).
 - 28 E. Goulielmakis, Z.-H. Loh, A. Wirth, R. Santra, N. Rohringer, V. S. Yakovlev, S. Zherebtsov, T. Pfeifer, A. M. Azzeer, M. F. Kling, et al., “Real-time observation of valence electron motion,” *Nature* **466**, 739–743 (2010).
 - 29 A. R. Attar, A. Bhattacharjee, C. Pemmaraju, K. Schnorr, K. D. Closser, D. Prendergast, and S. R. Leone, “Femtosecond x-ray spectroscopy of an electrocyclic ring-opening reaction,” *Science* **356**, 54–59 (2017).
 - 30 A. D. Smith, T. Balciunas, Y.-P. Chang, C. Schmidt, K. Zinchenko, F. B. Nunes, E. Rossi, V. Svoboda, Z. Yin, J.-P. Wolf, and H. J. Wörner, “Femtosecond soft-x-ray absorption spectroscopy of liquids with a water-window high-harmonic source,” *J. Phys. Chem. Lett.* **11**, 1981–1988 (2020).
 - 31 D. Garratt, L. Misiak, D. Wood, E. W. Larsen, M. Matthews, O. Alexander, P. Ye, S. Jarosch, C. Ferchaud, C. Strüber, et al., “Direct observation of ultrafast exciton localization in an organic semiconductor with soft x-ray transient absorption spectroscopy,” *Nat. Commun.* **13**, 3414 (2022).
 - 32 G. Fan, K. Legare, V. Cardin, X. Xie, R. Safaei, E. Kaksis, G. Andriukaitis, A. Pugzlys, B. Schmidt, J. Wolf, et al., “Ultrafast magnetic scattering on ferrimagnets enabled by a bright yb-based soft x-ray source,” *Optica* **9**, 399–407 (2022).
 - 33 B. Buras, J. Chwaszczewska, S. Szarras, and Z. Szmíd, “Fixed angle scattering (FAS) method for x-ray crystal structure analysis,” Report No. 894/H/PS, Institute of Nuclear Research, Warsaw, 10 (1968).
 - 34 B. C. Giessen and G. E. Gordon, “X-ray Diffraction: New High-Speed Technique Based on X-ray Spectrography,” *Science* (80-). **159**, 973–975 (1968).
 - 35 R. G. Moore, W. S. Lee, P. S. Kirchman, Y. D. Chuang, A. F. Kemper, M. Trigo, L. Patthey, D. H. Lu, O. Krupin, M. Yi, D. A. Reis, D. Doering, P. Denes, W. F. Schlotter, J. J. Turner, G. Hays, P. Hering, T. Benson, J.-H. Chu, T. P. Devereaux, I. R. Fisher, Z. Hussain, and Z.-X. Shen, “Ultrafast resonant soft x-ray diffraction dynamics of the charge density wave in TaTe_2 ,” *Phys. Rev. B* **93**, 024304 (2016).
 - 36 N. Thielemann-Kühn, D. Schick, N. Pontius, C. Trabant, R. Mitzner, K. Holldack, H. Zabel, A. Föhlich, and C. Schüßler-Langeheine, “Ultrafast and energy-efficient quenching of spin order: Antiferromagnetism beats ferromagnetism,” *Phys. Rev. Lett.* **119**, 197202 (2017).
 - 37 M. Mitrano, S. Lee, A. A. Husain, L. Delacretaz, M. Zhu, G. de la Peña Muñoz, S. X.-L. Sun, Y. I. Joe, A. H. Reid, S. F. Wandel, et al., “Ultrafast time-resolved x-ray scattering reveals diffusive charge order dynamics in $\text{La}_2\text{-x Ba}_x \text{CuO}_4$,” *Sci. Adv.* **5**, eaax3346 (2019).
 - 38 J.-Y. Chauleau, T. Chirac, S. Fusil, V. Garcia, W. Akhtar, J. Tranchida, P. Thibaudeau, I. Gross, C. Blouzon, A. e. Finco, et al., “Electric and antiferromagnetic chiral textures at multiferroic domain walls,” *Nature Mater.* **19**, 386–390 (2020).
 - 39 M. Hennecke, D. Schick, T. Sidiropoulos, F. Willems, A. Heilmann, M. Bock, L. Ehrentraut, D. Engel, P. Hessing, B. Pfau, et al., “Ultrafast element- and depth-resolved magnetization dynamics probed by transverse magneto-optical Kerr effect spectroscopy in the soft x-ray range,” *Phys. Rev. Research* **4**, L022062 (2022).
 - 40 T. Feng, A. Heilmann, M. Bock, L. Ehrentraut, T. Witting, H. Yu, H. Stiel, S. Eisebitt, and M. Schnürer, “27 w 2.1 μm OPCPA system for coherent soft x-ray generation operating at 10 kHz,” *Opt. Express* **28**, 8724–8733 (2020).
 - 41 M. van Mörbeck-Bock, T. Feng, A. Heilmann, L. Ehrentraut, H. Stiel, M. Hennecke, T. Sidiropoulos, C. von Korff Schmising, S. Eisebitt, and M. Schnürer, “High average power OPCPA MIR-systems for coherent soft x-ray generation accessing absorption edges of metals,” in *High Power Lasers and Applications*, Vol. 11777, International Society for Optics and Photonics (SPIE, 2021) p. 117770C.
 - 42 A.-L. Hamon, J. Verbeeck, D. Schryvers, J. Benedikt, and R. M. vd Sanden, “ElNES study of carbon k-edge spectra of plasma deposited carbon films,” *J. Mater. Chem.* **14**, 2030–2035 (2004).
 - 43 F. Frati, M. O. Hunault, and F. M. De Groot, “Oxygen k-edge x-ray absorption spectra,” *Chem. Rev.* **120**, 4056–4110 (2020).
 - 44 D. Stearns, M. Stearns, Y. Cheng, J. Stith, and N. Ceglio, “Thermally induced structural modification of mo-si multilayers,” *J. Appl. Phys.* **67**, 2415–2427 (1990).
 - 45 S. Andreev, S. Gaponov, S. Gusev, M. Haidl, E. Klunov, K. Prokhorov, N. Polushkin, E. Sadova, N. Salashchenko, L. Suslov, et al., “The microstructure and x-ray reflectivity of mo/si multilayers,” *Thin Solid Films* **415**, 123–132 (2002).
 - 46 S. Sakhonenkov, E. O. Filatova, A. U. Gaisin, S. A. Kasatikov, A. S. Konashuk, R. S. Pleshkov, and N. I. Chkhalo, “Angle resolved photoelectron spectroscopy as applied to x-ray mirrors: an in depth study of mo/si multilayer systems,” *Phys. Chem. Chem. Phys.* **21**, 25002–25010 (2019).
 - 47 D. Schick, S. Eckert, N. Pontius, R. Mitzner, A. Föhlich, K. Holldack, and F. Sorgenfrei, “Versatile soft x-ray-optical cross-correlator for ultrafast applications,” *Struct. Dyn.* **3** (2016), 10.1063/1.4964296.
 - 48 M. Elzo, E. Jal, O. Bunau, S. Grenier, Y. Joly, A. Ramos, H. Tolentino, J.-M. Tonnerre, and N. Jaouen, “X-ray resonant magnetic reflectivity of stratified magnetic structures: Eigenwave for-

- malism and application to a w/fe/w trilayer,” *Journal of Magnetism and Magnetic Materials* **324**, 105–112 (2012).
- ⁴⁹D. Schick, “udkm1Dsim—a Python toolbox for simulating 1D ultrafast dynamics in condensed matter,” *Comput. Phys. Commun.* **266**, 108031 (2021).
- ⁵⁰D. Kriegner, E. Wintersberger, and J. Stangl, “Xrayutilities: A versatile tool for reciprocal space conversion of scattering data recorded with linear and area detectors,” *J. Appl. Cryst.* **46**, 1162–1170 (2013).
- ⁵¹L. Sève, J. Tonnerre, and D. Raoux, “Determination of the anomalous scattering factors in the soft-x-ray range using diffraction from a multilayer,” *J. Appl. Cryst.* **31**, 700–707 (1998).
- ⁵²D. Attwood, *Soft x-rays and extreme ultraviolet radiation: principles and applications* (Cambridge university press, 2000).
- ⁵³M. Magnuson and C. F. Hague, “Determination of the refractive index at soft x-ray resonances,” *J. Electron Spectrosc. Relat. Phenom.* **137**, 519–522 (2004).
- ⁵⁴A. Bartels, T. Dekorsy, H. Kurz, and K. Köhler, “Coherent zone-folded longitudinal acoustic phonons in semiconductor superlattices: Excitation and detection,” *Phys. Rev. Lett.* **82**, 1044–1047 (1999).
- ⁵⁵M. Bargheer, N. Zhavoronkov, Y. Gritsai, J. Woo, D. Kim, M. Wörner, and T. Elsaesser, “Coherent atomic motions in a nanostructure studied by femtosecond x-ray diffraction,” *Science* **306**, 1771–1773 (2004).
- ⁵⁶C. Thomsen, H. T. Grahn, H. J. Maris, and J. Tauc, “Surface generation and detection of phonons by picosecond light pulses,” *Phys. Rev. B* **34**, 4129 (1986).
- ⁵⁷G. Tas and H. J. Maris, “Electron diffusion in metals studied by picosecond ultrasonics,” *Phys. Rev. B* **49**, 15046–15054 (1994).
- ⁵⁸P. Ruello and V. E. Gusev, “Physical mechanisms of coherent acoustic phonons generation by ultrafast laser action,” *Ultrasonics* **56**, 21–35 (2015).
- ⁵⁹M. Mattern, A. von Reppert, S. P. Zeuschner, M. Herzog, J.-E. Pudell, and M. Bargheer, “Concepts and use cases for picosecond ultrasonics with x-rays,” *Photoacoustics*, 100503 (2023).
- ⁶⁰M. Holtz, C. Hauf, J. Weisshaupt, A.-A. H. Salvador, M. Woerner, and T. Elsaesser, “Towards shot-noise limited diffraction experiments with table-top femtosecond hard x-ray sources,” *Struct. Dyn.* **4**, 054304 (2017).
- ⁶¹D. Schick, F. Steinbach, T. Noll, C. Strüber, D. Engel, C. von Korff Schmising, B. Pfau, and S. Eisebitt, “High-speed spatial encoding of modulated pump–probe signals with slow area detectors,” *Meas. Sci. Technol.* **32**, 025901 (2021).
- ⁶²A. Choudhury and C. Brooks, “Contributions to the heat capacity of solid molybdenum in the range 300–2890 k,” *International journal of thermophysics* **5**, 403–429 (1984).
- ⁶³H. Abe, H. Kato, and T. Baba, “Specific heat capacity measurement of single-crystalline silicon as new reference material,” *Japanese Journal of Applied Physics* **50**, 11RG01 (2011).
- ⁶⁴S. Wen, J. Ma, A. Kundu, and W. Li, “Large lattice thermal conductivity, interplay between phonon-phonon, phonon-electron, and phonon-isotope scatterings, and electrical transport in molybdenum from first principles,” *Phys. Rev. B* **102**, 064303 (2020).
- ⁶⁵D. R. Queen, X. Liu, J. Karel, T. H. Metcalf, and F. Hellman, “Excess specific heat in evaporated amorphous silicon,” *Phys. Rev. Lett.* **110**, 135901 (2013).
- ⁶⁶M. Ashghi, M. Touzelbaev, K. Goodson, Y. Leung, and S. Wong, “Temperature-dependent thermal conductivity of single-crystal silicon layers in soi substrates,” *ASME. J. Heat Transfer* **120**, 30–36 (1998).
- ⁶⁷G. White, T. Smith, and R. Carr, “Thermal expansion of cr, mo and w at low temperatures,” *Cryogenics* **18**, 301–303 (1978).
- ⁶⁸J. Dickinson and P. Armstrong, “Temperature dependence of the elastic constants of molybdenum,” *Journal of applied Physics* **38**, 602–606 (1967).
- ⁶⁹M. de Lima Jr, R. Lacerda, J. Vilcarromero, and F. Marques, “Coefficient of thermal expansion and elastic modulus of thin films,” *Journal of Applied Physics* **86**, 4936–4942 (1999).
- ⁷⁰M. A. Hopcroft, W. D. Nix, and T. W. Kenny, “What is the young’s modulus of silicon?” *Journal of microelectromechanical systems* **19**, 229–238 (2010).
- ⁷¹E. Dechaumphai, D. Lu, J. J. Kan, J. Moon, E. E. Fullerton, Z. Liu, and R. Chen, “Ultralow thermal conductivity of multilayers with highly dissimilar debye temperatures,” *Nano letters* **14**, 2448–2455 (2014).
- ⁷²W. S. Werner, K. Glantschnig, and C. Ambrosch-Draxl, “Optical constants and inelastic electron-scattering data for 17 elemental metals,” *Journal of Physical and Chemical Reference Data* **38**, 1013–1092 (2009).
- ⁷³D. T. Pierce and W. E. Spicer, “Electronic structure of amorphous silicon from photoemission and optical studies,” *Phys. Rev. B* **5**, 3017–3029 (1972).
- ⁷⁴H. Li, “Refractive index of silicon and germanium and its wavelength and temperature derivatives,” *Journal of Physical and Chemical Reference Data* **9**, 561–658 (1980).
- ⁷⁵S.-S. Wellershoff, J. Hohlfeld, J. Güdde, and E. Matthias, “The role of electron–phonon coupling in femtosecond laser damage of metals,” *Appl. Phys. A* **69**, S99–S107 (1999).
- ⁷⁶L. Barreau, A. D. Ross, V. Kimberg, P. Krasnov, S. Blinov, D. M. Neumark, and S. R. Leone, “Core-excited states of sf_6 probed with soft-x-ray femtosecond transient absorption of vibrational wave packets,” *Phys. Rev. A* **108**, 012805 (2023).
- ⁷⁷M.-C. Chen, P. Arpin, T. Popmintchev, M. Gerrity, B. Zhang, M. Seaberg, D. Popmintchev, M. M. Murnane, and H. C. Kapteyn, “Bright, coherent, ultrafast soft x-ray harmonics spanning the water window from a tabletop light source,” *Phys. Rev. Lett.* **105**, 173901 (2010).
- ⁷⁸A. Di Cicco, G. Polzoni, R. Gunnella, A. Trapananti, M. Minicucci, S. Rezvani, D. Catone, L. Di Mario, J. Pelli Cresi, S. Turchini, et al., “Broadband optical ultrafast reflectivity of si, ge and gaas,” *Sci. Rep.* **10**, 17363 (2020).
- ⁷⁹J. Fabian and P. B. Allen, “Thermal expansion and grüneisen parameters of amorphous silicon: A realistic model calculation,” *Physical review letters* **79**, 1885 (1997).
- ⁸⁰R. J. Green, V. Zabolotnyy, M. Zwiebler, Z. Liao, S. Macke, R. Sutarto, F. He, M. Huijben, G. Rijnders, G. Koster, J. Geck, V. Hinkov, and G. A. Sawatzky, “Intrinsic versus extrinsic orbital and electronic reconstructions at complex oxide interfaces,” *Phys. Rev. Mater.* **5**, 065004 (2021).
- ⁸¹H. He, A. Gray, P. Granitzka, J. Jeong, N. P. Aetukuri, R. Kukreja, L. Miao, S. A. Breitweiser, J. Wu, Y. Huang, et al., “Measurement of collective excitations in VO_2 by resonant inelastic x-ray scattering,” *Phys. Rev. B* **94**, 161119 (2016).
- ⁸²M. Hepting, R. J. Green, Z. Zhong, M. Bluschke, Y. E. Suyolcu, S. Macke, A. Frano, S. Catalano, M. Gibert, R. Sutarto, F. He, G. Cristiani, G. Logvenov, Y. Wang, P. A. van Aken, P. Hansmann, M. Le Tacon, J.-M. Triscone, G. A. Sawatzky, B. Keimer, and E. Benckiser, “Complex magnetic order in nickelate slabs,” *Nat. Physics* **14**, 1097–1102 (2018).
- ⁸³C. Kleine, M.-O. Winghart, Z.-Y. Zhang, M. Richter, M. Eki-mova, S. Eckert, M. J. J. Vrakking, E. T. J. Nibbering, A. Rouzée, and E. R. Grant, “Electronic state population dynamics upon ultrafast strong field ionization and fragmentation of molecular nitrogen,” *Phys. Rev. Lett.* **129**, 123002 (2022).
- ⁸⁴L. Maerten, A. Bojahr, and M. Bargheer, “Observing backfolded and unfolded acoustic phonons by broadband optical light scattering,” *Ultrasonics* **56**, 148–152 (2015).
- ⁸⁵T. Popmintchev, M.-C. Chen, D. Popmintchev, P. Arpin, S. Brown, S. Ališauskas, G. Andriukaitis, T. Balčiūnas, O. D. Mücke, A. Pugzlys, et al., “Bright coherent ultrahigh harmonics in the kev x-ray regime from mid-infrared femtosecond lasers,” *Science* **336**, 1287–1291 (2012).
- ⁸⁶R. Schoenlein, T. Elsaesser, K. Holldack, Z. Huang, H. Kapteyn, M. Murnane, and M. Woerner, “Recent advances in ultrafast x-ray sources,” *Phil. Trans. R. Soc. A* **377**, 20180384 (2019).
- ⁸⁷D. A. Shapiro, Y.-S. Yu, T. Tylliszczak, J. Cabana, R. Celestre, W. Chao, K. Kaznatcheev, A. D. Kilcoyne, F. Maia, S. Marchesini, et al., “Chemical composition mapping with nanometre

- resolution by soft x-ray microscopy,” *Nature Photon.* **8**, 765–769 (2014).
- ⁸⁸L. Vidas, C. M. Günther, T. A. Miller, B. Pfau, D. Perez-Salinas, E. Martínez, M. Schneider, E. Gührs, P. Gargiani, M. Valvidares, R. E. Marvel, K. A. Hallman, R. F. Haglund Jr., S. Eisebitt, and S. Wall, “Imaging nanometer phase coexistence at defects during the insulator–metal phase transformation in VO_2 thin films by resonant soft X-ray holography,” *Nano Lett.* **18**, 3449–3453 (2018).
- ⁸⁹C. von Korff Schmising, B. Pfau, M. Schneider, C. M. Günther, M. Giovannella, J. Perron, B. Vodungbo, L. Müller, F. Capotondi, E. Pedersoli, N. Mahne, J. Lüning, and S. Eisebitt, “Imaging ultrafast demagnetization dynamics after a spatially localized optical excitation,” *Phys. Rev. Lett.* **112**, 217203 (2014).
- ⁹⁰Y. Yang, R. E. Mainz, G. M. Rossi, F. Scheiba, M. A. Silva-Toledo, P. D. Keathley, G. Cirmi, and F. X. Kärtner, “Strong-field coherent control of isolated attosecond pulse generation,” *Nat. Commun.* **12**, 6641 (2021).
- ⁹¹K. Yao, F. Willems, C. von Korff Schmising, C. Strüber, P. Hensing, B. Pfau, D. Schick, D. Engel, K. Gerlinger, M. Schneider, *et al.*, “A tabletop setup for ultrafast helicity-dependent and element-specific absorption spectroscopy and scattering in the extreme ultraviolet spectral range,” *Rev. Sci. Instrum.* **91** (2020), 10.1063/5.0013928.
- ⁹²K.-J. Zhou, M. Radovic, J. Schlappa, V. Strocov, R. Frison, J. Mesot, L. Patthey, and T. Schmitt, “Localized and delocalized Ti 3d carriers in $LaAlO_3/SrTiO_3$ superlattices revealed by resonant inelastic x-ray scattering,” *Phys. Rev. B* **83**, 201402 (2011).
- ⁹³K. S. Zinchenko, F. Ardana-Lamas, V. U. Lanfaloni, T. T. Luu, Y. Pertot, M. Huppert, and H. J. Wörner, “Apparatus for attosecond transient-absorption spectroscopy in the water-window soft-x-ray region,” *Sci. Rep.* **13**, 3059 (2023).
- ⁹⁴M. Zwiebler, E. Di Gennaro, J. Hamann-Borrero, T. Ritschel, R. Green, G. Sawatzky, E. Schierle, E. Weschke, A. Leo, F. M. Granozio, *et al.*, “Transition from a uni- to a bimodal interfacial charge distribution in $LaAlO_3/SrTiO_3$ upon cooling,” *Sci. Rep.* **10**, 18359 (2020).